RSC Advances

PAPER

View Article Online
View Journal | View Issue

Cite this: *RSC Adv.*, 2025, **15**, 16267

Legume root nodule derived porous carbon materials through the *in situ* ZIF-8 activation strategy†

Minyu Li, *[b] Yifan Zhou,[ab] Lingling Lin[b] and Wenmu Li *[c]

The utilization of harsh chemicals is obligatory during the preparation of biomass-derived carbon materials. ZIF-8 serves as a zinc-based metal–organic framework (MOF), in which the internal zinc ions (Zn^{2+}) are reduced to metallic Zn during high-temperature pyrolysis, which then evaporates and etches the carbon skeleton, significantly increasing the specific surface area and porosity of the material. In the current work, the ZIF-8 and the legume root nodules were used as an activator and biomass precursors to develop a more atom-economical and eco-friendly strategy for the preparation of porous carbon materials. The roles the ZIF-8 and the species of legume root nodules play in the structure and performance of the final carbon materials were well explored and discussed. The specific surface area of our optimal carbon RW@Z8(5) is up to 1459.27 $m^2\ g^{-1}$. The catalyst RW@Z8(5) was employed in fuel cells for the oxygen reduction reaction (ORR) and demonstrated a half-wave potential ($E_{1/2}$) of 0.720 V (*vs.* RHE) in 0.1 M $HClO_4$, which is only 88 mV lower than that of the Pt/C catalyst. Our results prove the possibility of the metal–organic framework (MOF) activation strategy for the development of biomass-derived porous carbon materials.

Received 8th March 2025
Accepted 6th May 2025

DOI: 10.1039/d5ra01675d

rsc.li/rsc-advances

Introduction

Biomass is regarded as an ideal precursor for the preparation of multifunctional carbon materials owing to its environmentally friendly renewability and unique chemical composition.[1–3] Its primary components are carbohydrates, which can form a porous structure during the pyrolysis process by self-doping with heteroatoms like Fe, N, and Mo. This offers a natural advantage for the targeted design of functional carbon materials.[4–6] Controlling the pyrolysis and activation processes enables biomass-derived carbon materials to precisely form hierarchical pore structures (micro/meso/macropores in synergy),[7,8] which endow them with excellent electrical conductivity, high specific surface area, and outstanding cycling stability. These characteristics render them highly promising for applications in various fields, such as CO_2 adsorption (with CO_2 uptake as high as 5 mmol g^{-1}), lithium-sulfur battery separators (with suppression of polysulfide shuttle effect), and fuel cell catalysts (with enhanced electrochemical activity).[9–13] However, the chemical heterogeneity of biomass precursors makes the carbonization process difficult to control precisely. The transformation of renewable biomass into innovative carbon-based materials and the control of their functionality remain a significant challenge.[14,15]

To convert biomass into high-quality porous carbon materials, many methods have been developed, such as hydrothermal carbonization, chemical activation, hard and soft templates, and so on.[16,17] Among them, the chemical activation method can effectively increase the number of micropores and mesopores of biomass carbon material to improve the transmission efficiency. It can also control the porosity of carbon materials and obtain porous carbon materials with uniform pore size.[16] Many harsh chemicals, like KOH, H_3PO_4, $ZnCl_2$, and others, are frequently utilized in chemical activation techniques.[18–20] Different activators have slight differences in activation mechanisms. KOH operates as an oxidizing agent, while H_3PO_4 and $ZnCl_2$ primarily carry out dehydration processes.[21] The chemical activators increase the degree of surface defects, porosity, and specific surface area of carbon materials through a series of integrated and synergistic effects. These effects include the distortion of the carbon lattice to create a microporous structure, the insertion of metal into carbon layer, and the creation of multilevel pore structures by etching the carbon skeleton.[22] The usage of KOH serves as an oxidizing agent, converting carbon into carbonate. This method leads to the production of pores in the carbon framework due to

[a]*College of Chemistry, Fuzhou University, Fuzhou 350108, P. R. China*
[b]*Fujian Provincial Key Laboratory of Featured Materials in Biochemical Industry, Fujian Province University Key Laboratory of Green Energy and Environment Catalysis, College of New Energy and Materials, Ningde Normal University, Fujian 352100, China. E-mail: liminyu90@126.com*
[c]*Key Laboratory of Optoelectronic Materials Chemistry and Physics, Fujian Institute of Research on the Structure of Matter, Chinese Academy of Sciences, China. E-mail: liwm@fjirsm.ac.cn*

† Electronic supplementary information (ESI) available. See DOI: https://doi.org/10.1039/d5ra01675d

etching, promoting the development of microporous structures.[23] H_3PO_4 reacts primarily with carbon fragments, removing oxygen and forming vacancies, which leads to non-homogeneous pore size. In contrast, $ZnCl_2$ produces a uniform pore size due to its hydrate or small molecular size.[24,25] Additionally, the solvation effect of $ZnCl_2$ promotes the breaking of lateral bonds in cellulose molecules, etching the carbon material to form abundant inter- and intra-pore spaces.[26,27] Thus, $ZnCl_2$ facilitates the formation of a uniform mesoporous structure compared to other activators.[28] However, chemical activation has several drawbacks, such as the need for a high acid cleaning process and the extreme corrosiveness of commonly used agents like H_3PO_4 and KOH, which are non-recyclable.[2,14,28,29] Thus, the use of harsh chemicals as pore-opening agents conflicts with the goals of eco-friendliness and atom-economy. Meanwhile, chemical activation converts the biomass into a porous carbon material, where the structure is a combination of amorphous and crystalline carbon.[17] Amorphous carbon exhibits a wide range of surface functional groups and high specific surface area, which can provide abundant loading sites for the catalyst and make the catalyst particles dispersed uniformly.[30] However, the electrical conductivity as well as the chemical stability of the carbon material with a high degree of disorder will be inferior to that of highly crystalline graphitic carbon.[31] Thus, the overall catalytic performance can be further enhanced by optimizing the ratio of crystalline and amorphous graphitic carbon in porous carbon materials.

In recent years, the zeolite imidazolate framework (ZIF-8) has been recognized as a novel porous material.[32,33] Besides its applications in gas separation, energy storage, and sensing, ZIF-8 is also used in catalysis as an efficient support for metal atoms.[34] This is owing to its tunable particle size, large surface area, microporosity, remarkable heat stability, and distinctive spatial organization.[35,36] When calcined at around 900 °C, the zinc ions (Zn^{2+}) in ZIF-8 was reduced to metallic zinc (Zn), which then etched the carbon material through evaporation.[37–39] Meanwhile, the structure of the regular dodecahedron of ZIF-8 is retained intact, which increases the ratio of graphitization of the porous carbon material.[35,40] Thus, using ZIF-8 as a pore-opening method to activate biomass-derived carbon materials is more economical and ecologically friendly compared to traditional harsh chemicals.

In recent years, the application of biomass-derived porous carbon materials in proton exchange membrane fuel cells (PEMFCs) has shown great potential, especially in replacing precious metal catalysts (PMCs) for oxygen reduction reaction (ORR).[41–44] For instance, Wang *et al.* synthesized N-, P-, and Fe tri-doped nanoporous carbon from corn husk, achieving superior ORR activity, enhanced stability, and stronger methanol tolerance compared to commercial Pt/C in 0.1 M KOH.[45] Zhou *et al.* prepared porous carbon materials with graphene-like nanosheet structures by KOH activation of biomass eggplant, exhibiting ORR performance comparable to Pt/C in alkaline media.[46] Liu *et al.* employed $ZnCl_2$ activation and subsequent H_2SO_4 washing to produce carbon-based catalysts from soybean biomass, with onset and half-wave potentials nearly matching those of Pt/C.[29] Overall, biomass-derived carbon materials can rival noble metal catalysts in alkaline media; however, their performance remains significantly limited under the acidic conditions required for practical PEMFC operation.[37,47] Our previous work demonstrated that highly efficient ORR catalysts could be prepared by $ZnCl_2$ activation of legume root nodules. However, this strategy relies on acid washing to remove residual metal ions and oxides in the pores, a process that not only reduces active site density but also poses environmental contamination risks.[48] The legume root nodules, which contain atomically dispersed metal sites Fe and Mo coordinated through elements N and S,[48–51] are inherent multi-metal catalytical biomass precursors. In the current work, the ZIF-8 was grown *in situ* on the pre-carbonized legume root nodules and used as an activator to replace the harsh chemicals for the preparation of biomass-derived porous carbon materials. In addition, the catalytic activity of the prepared catalysts in the oxidative raw reaction (ORR) was thoroughly investigated. Our results prove the possibility of the metal–organic framework materials activation strategy for the development of biomass-derived carbon materials.

Experiment

Materials

$Zn(NO_3)_2 \cdot 6H_2O$ (99%), methanol (99%), and 2-methylimidazole (98%), were purchased from Sinopharm Chemical Reagent Co., Ltd. Legume root nodules were obtained from different areas. All chemicals and materials were used without further purification.

Catalysts preparation

Four legume root nodules with high nitrogen content were selected for the experiment: White lentil, Soybean, Lentil, and Knife Beans (named W, S, L, and K, respectively). The rhizomes were washed with ultrapure water to remove the outer skin and impurities, followed by drying at 120 °C for 10 hours. Subsequently, the dried rhizomes were carbonized at 350 °C for 2 hours under an argon flow to achieve complete carbonization. Afterward, the carbonized rhizomes were subjected to ball milling to obtain the black carbon powder RN350 (N═W, S, L, and K).

2.271 g of zinc nitrate hexahydrate and 166 mg of RW350 (nodular carbonation) were dissolved in 75 mL of methanol using the hydrothermal synthesis process. The mixture was then heated and stirred at 60 °C to ensure uniform distribution. There were 2.683 g of 2-methylimidazole in the other 75 mL methanol solution. The two solutions were combined and heated and stirred at 60 °C for 40 hours. Through the centrifugation process and wash the precipitate with ethanol, followed by vacuum drying for 12 hours at 60 °C degrees state. The resulting RW@ZIF-8(5) blend, with a mass ratio of RW350 to ZIF-8 of 1 : 5, was then prepared by fine grinding. Finally, the blend was pyrolyzed for two hours at temperatures between 800 and 1100 °C while being heated at a rate of 5 °C per minute using an argon flow. The black powder was ground to obtain RW@Z8(5)-*T* (where *T* represents 800, 900, 1000, and 1100 °C).

For comparison, RW-1000, RW@Z8(1), RW@Z8(2), and RW@Z8(10) represent the direct pyrolysis of RW350 powder for

2 h under an Ar atmosphere at 1000 °C and the mass ratios of RW350 and ZIF-8 of 1 : 1, 1 : 2, and 1 : 10 at 1000 °C under Ar atmosphere, respectively. The catalysts were prepared by pyrolysis for 2 h. Additionally, three more catalysts were synthesized using rhizobia from three different legumes as precursors, in combination with ZIF-8, to investigate the effect of various legumes on ORR. The obtained catalysts are denoted as RS@Z8(5), RL@Z8(5), and RK@Z8(5), respectively, and the preparation method is the same as RW@Z8(5).

Characterization

The micro-morphology of the catalysts was investigated by field emission scanning electron microscopy (FESEM) (SU8010) and field emission transmission electron microscopy (FETEM) (Tecnai G2 F20 S-TWIN). A MiniFlex-II diffractometer (Rigaku, Japan) was used to perform powder X-ray diffraction (XRD) patterns. Use of Raman spectra (Renishaw 2000) for testing the graphitization of catalysts. The specific surface area and pore size distribution of samples were examined using the Brunauer–Emmett–Teller (BET, Micromeritics) technique. A device called an ESCALAB 250Xi was used to perform X-ray photoelectron spectroscopy (XPS) observations. A Vario EL Cube was used to collect measurements for elemental analysis (EA). Using inductively coupled plasma emission spectrometry (ICP, Ultima-2) to identify trace elements in samples.

Electrochemical measurements

The rotating disk electrode (RDE) and rotating ring disk electrode (RRDE) were used as the working electrodes, graphite as the counter electrode, and KCl-saturated Ag/AgCl as the reference electrode. These electrodes were linked to the CHI-760E electrochemical workstation to perform electrochemical tests in a three-electrode system. The conversion of electrochemically measured potentials to reversible hydrogen electrodes (RHE) using the Nernst equation:

$$E_{RHE} = E_{Ag/AgCl} + 0.059\ pH + 0.197\ V \quad (1)$$

The catalyst powder (4 mg), Nafion (30 μL, 5 wt%) solution, deionized water (416 μL), and isopropanol (550 μL) were mixed and sonicated for 1 hour to form an ink. Then, 10 μL of the ink was loaded onto the glassy carbon electrode to obtain a loading of 200 μg cm^{-2} and dried naturally at room temperature.

The cyclic voltammetry (CV) and linear scanning voltammetry (LSV) in O_2-saturated 0.1 M $HClO_4$ solution at a scanning rate of 10 mV s^{-1} to study the electrochemical properties of catalysts. The LSV curve was obtained by subtracting the nitrogen background. The K–L equation was used to compute the electrochemical catalytic route from LSV data that RDE had recorded at various speeds. Four-electron selectivity and peroxide yield were obtained at 0.6 V (*vs.* HER) using the RRDE. Catalyst durability and methanol tolerance tests were performed using the *i–t* chronoamperometry approach.

Results and discussion

The process for synthesizing RN@Z8(*x*) porous catalysts from biomass legume root nodules is shown in Fig. 1. The *x* in RN@Z8(*x*) represents the initial weight ratio of ZIF-8 to the root nodules. The N stands for legume root nodules of the White lentil (W), Soybean (S), Lentil (L), and Knife bean (K). Most of

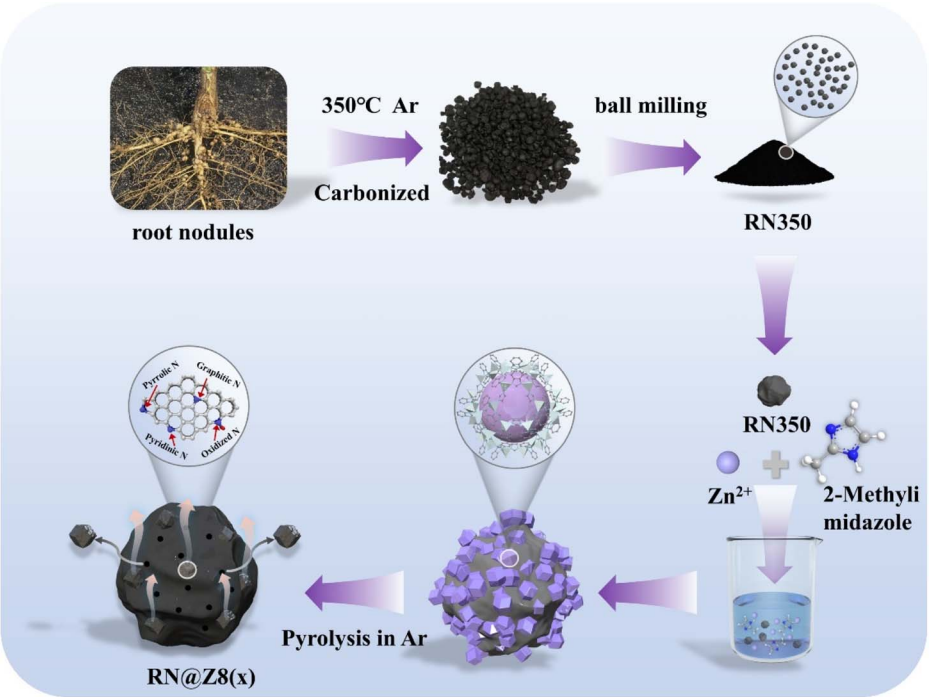

Fig. 1 Schematic of the procedure of fabrication of RN@Z8(*x*) from biomass legume root nodules.

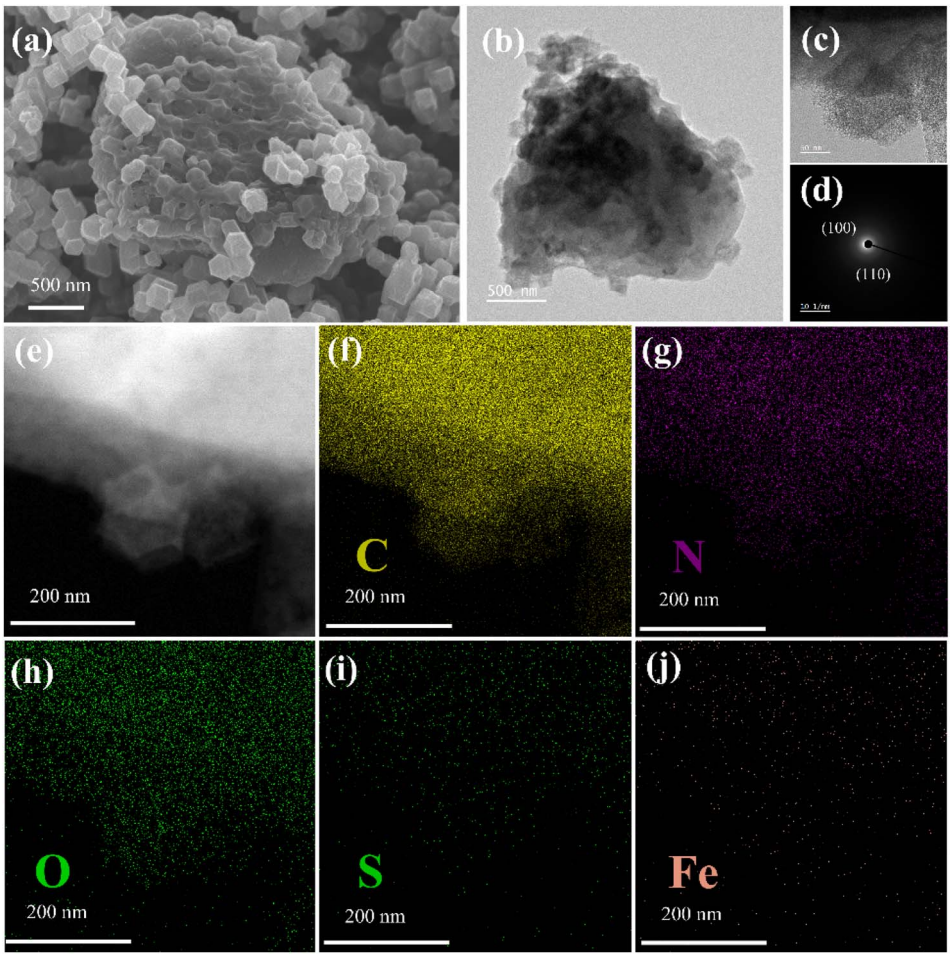

Fig. 2 (a) SEM (b) TEM (c) HRTEM, and (d) SAED images of RW@Z8(5). (e) HAADF-STEM image of RW@Z8(5). The corresponding elemental mapping images of (f) C, (g) N, (h) O, (i) S, and (j) Fe. (The content of S and Mo atoms in root nodules is very small, and it is difficult to distinguish between S and Mo elements by EDS mapping; therefore, we do not show the mapping images of Mo elements in figure).

our RN@Z8(x) catalysts were synthesized under 1000 °C heat treatment, unless otherwise specified.

Fig. 2a–c show typical SEM, TEM, and HRTEM images of RW@Z8(5). The large number of characteristic dodecahedral structures in ZIF-8, anchoring on or embedding in the legume root nodules before and after calcination, was clearly observed. The zinc in ZIF-8 evaporates and etches the root nodules during high-temperature treatment. It thus acts as a pore-forming agent. Numerous nanoscale pores contained in the disordered carbon layer are seen in the photos, indicating that ZIF-8 added to the legume root nodules greatly increases the carbon material's porosity and electrical conductivity, improving the catalyst's performance (RW@Z8(5)). The selected-area electron diffraction (SAED) pattern (Fig. 2d) distinctly reveals two diffraction rings representing the (100) and (110) crystallographic planes of graphite. The HAADF-STEM was applied to explicate the element composition of RW@Z8(5). Fig. 2f–j displays the matching EDS mapping image for the elements C, N, O, S, and Fe. In particular, trace amounts of S and Mo atoms are difficult to discern using EDS mapping analysis. The EDS mapping of Mo elements is not shown here. The SEM images of three other catalysts RN@Z8(5) (N═S, L, and K) obtained from different types of legume root nodules are shown in Fig. S1.† No significant structural discrepancy was observed, indicating that the different types of legume root nodules do not significantly affect the spatial structure of the catalysts.

XRD was used to investigate the crystal structure of the produced samples. As illustrated in Fig. 3a, all RW@Z8(x) catalysts exhibit two separate wide diffraction peaks at 23.7° and 42.7°, which represent the graphite peaks of the (002) and (100) crystal planes, respectively. However, the RW-1000 catalyst's diffraction peak is at about 22.1°, which differs from that of the RW@Z8(x) catalyst, exhibiting a poorly graphitized (002) crystal surface. This suggests that the incorporation of ZIF-8 increases the graphitization of carbon in RW@Z8(5).[3,45] Due to the low concentrations of Fe, Mo, and S, or their incorporation into a disordered carbon framework, no distinct diffraction peaks for these elements are observed. To investigate the effect of temperature on graphitization, catalysts derived from white lentils (W) were prepared at various temperatures (Fig. S5(a)†). As a result, we found a slight deviation in the position of the characteristic peaks of the (002) crystal surface of the catalyst,

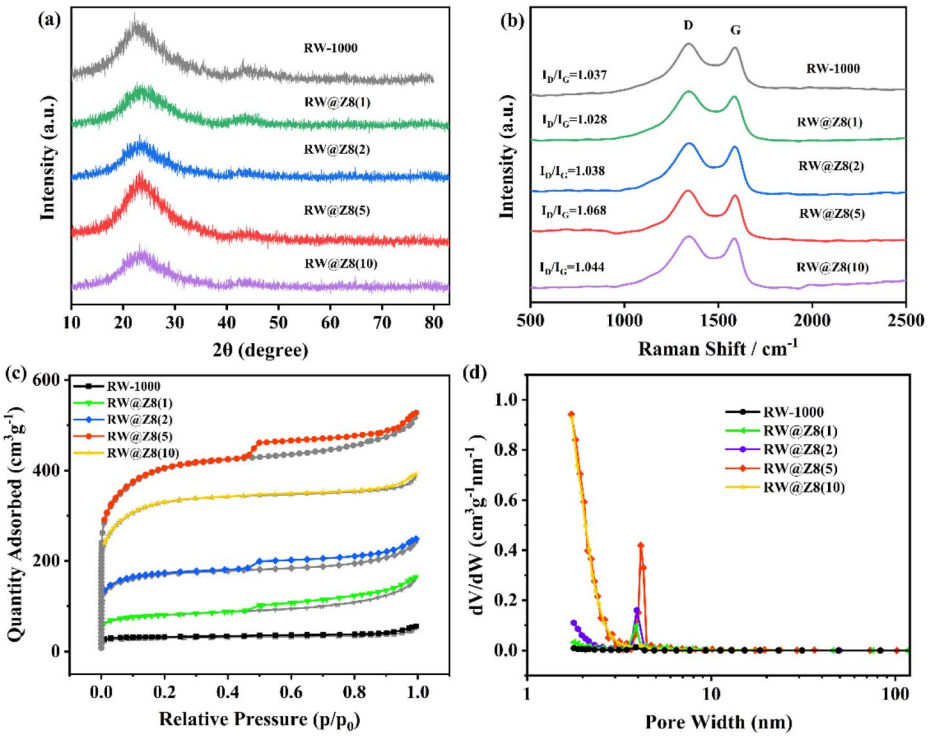

Fig. 3 (a) XRD pattern of RX@Z8(*x*), (b) Raman spectra with the corresponding I_D/I_G values, (c) N_2 adsorption–desorption isotherms, (d) corresponding pore size distributions.

which indicates that the degree of graphitization of the catalyst is affected by the temperature.

The catalysts were characterized by Raman spectroscopy for structural defects and graphitization structure. Carbon materials exhibit a D-band at 1343 cm^{-1}, which is a distinctive feature of their disordered structure, and a G-band at 1590 cm^{-1}, corresponding to the sp^2 hybridized graphitic structure. The degree of graphitization and defects in carbon materials are evaluated using the D-band/G-band intensity ratio (I_D/I_G). The I_D/I_G values of RW@Z8(*x*), as displayed in Fig. 3b, fall between 1.028 and 1.068, and they are strongly correlated with ZIF-8 loading. These results suggest that the degree of carbon skeleton defects increases with ZIF-8 loading, likely due to the etching of the carbon skeleton by ZIF-8, which facilitates the creation of more defects through *in situ* self-doping of heteroatoms. However, theI_D/I_G value decreases at higher loading due to a reduced concentration of heteroatoms. ZIF-8 etching of carbon material disrupts its regular structure, exposing more crystal edges with unique atomic coordination and electronic structure, which can provide active sites for reactions. Etching can not only create defects such as vacancies and dislocations, but also change the electron density distribution. Fig. S5(d)† shows the Raman test of catalysts prepared from different root nodules at the same temperature. As all root nodules are derived from beans, the carbon materials show a similar degree of graphitization during high-temperature pyrolysis. Among the root nodules of various beans, it is evident that RW@Z8(5) has the greatest I_D/I_G value. Our results indicated that the rhizobacteria do not affect the graphitization degree of the catalysts.

The catalysts' specific surface area was investigated using the Brunauer–Emmett–Teller (BET) method (Fig. 3c), and the corresponding pore size distribution was ascertained using the Barrett–Joyner–Halenda (BJH) approach (Fig. 3d). Table S1† summarizes the data on specific surface area, microporous/mesoporous area, average pore size values, and other relevant properties of catalysts produced with various ZIF-8 loadings. The mesopores of RW@Z8(*x*) increase with ZIF-8 loading, and their type-H4 hysteresis loop becomes more pronounced. The number of mesopores of RW@Z8(*x*) increases with the increasing loading of the activator ZIF-8, and their type-H4 hysteresis line is more obvious. The sample displays a typical type IV adsorption isotherm with a noticeable type-H4 hysteresis loop when the relative pressure p/p_o is between 0.45 and 1. According to adsorption isotherm theories, this phenomenon strongly suggests the presence of mesoporous structures in the prepared catalysts. The BET specific surface area of RW@Z8(*x*) ranged from 292.07 to 1459.27 $m^2\ g^{-1}$, significantly larger than that of RW-1000 (109.74 $m^2\ g^{-1}$), indicating that the inclusion of ZIF-8 promotes the formation of micro/mesopores and is strongly correlated with its loading. Fig. S7–S8† displays the pore size distributions and N_2 adsorption–desorption isotherms of RW@Z8(5) at various pyrolysis temperatures (800–1100 °C) and RN@Z8(5) from various root nodules (W, S, L, and K). Table S2–S3† displays the catalysts' specific surface areas and pore characteristics. Following the same procedure, the

RN@Z8(5) produced from several bean rhizomes showed comparable pore size distribution.

The elemental composition and surface chemical bonding were investigated using XPS. From the full XPS spectrum of Fig. 4b, it was observed that the catalyst RW-1000, which was not activated by ZIF-8, contained elements such as C, N, S, Br, and Ca. This shows that bean rhizomes may be made up of protein, cellulose, and trace amounts of inorganic minerals. High-resolution XPS spectra of RW-1000 revealed the details of N, S, Mo, and Fe elements (Fig. 4 and S9†), suggesting that leguminous rhizomes are promising precursors rich in heteroatoms. It can be observed through the high-resolution N1s XPS spectra of Fig. 4a that elemental N exhibits four different nitrogen species, namely pyridinic-N (398.4 ± 0.1 eV), pyrrolic-N (399.5 ± 0.2 eV), graphitic-N (401.1 ± 0.2 eV), and oxidized-N (402.7 ± 0.4 eV). XPS analysis was conducted on catalysts prepared with different ZIF-8 loadings, at different temperatures, and various bean species, as shown in Fig. S9–S14.† High-resolution XPS spectroscopy was used to show that self-doped N, S, Mo, and Fe were present inside the carbon matrix. The elemental composition in the made samples was measured by integrating the peak regions of each element's high-resolution spectra (Tables S4–S6†). Analyzing the elemental composition and electronic makeup of S, Mo, and Fe in RW@Z8(5) produced at various temperatures. As shown in Table S3,† the N content gradually decreased with increasing pyrolysis temperature. Furthermore, because of their distinct electrical structures and molecular configurations, graphitic-N and pyridinic-N are both acknowledged as catalytically active locations for redox reactions. As shown in Table S4,† the electrocatalysts synthesized at 1000 °C did not exhibit the highest N content. However, the relative content of pyridinic-N and graphitic-N was higher than that of catalysts prepared at lower pyrolysis temperatures. The concentration of pyridine-N and graphite-N decreases as ZIF-8 loading increases, according to a comparison of nitrogen in the RW@Z8(x) with variable ZIF-8 loading. Moreover, the heteroatom content in RW@Z8(5) is higher than that in RN@Z8(5) catalysts derived from various bean sources. In agreement with the XPS findings, elemental analysis (EA) and inductively coupled plasma (ICP) emission spectrometry (Tables S7–S9†) corroborated the contents of C, H, N, S, Fe, and Mo in the RW@Z8(x) catalysts. The influence of minor quantities of Br, Si, and Ca in precursor RN350 is insignificant since they are relatively inactive.

The activator loading and pyrolysis temperature are the primary factors influencing the ORR catalytic activity of biomass-derived catalysts. The cyclic voltammetry (CV) was used to evaluate the influence of activator loading and pyrolysis temperature on the electrochemical properties of the catalyst (Fig. 5a and S15a†). The catalyst RW@Z8(5), with a five-fold weight loading of ZIF-8 to RW350 pyrolyzed at 1000 °C, demonstrated superior oxygen reduction performance (cathode oxygen reduction peak potential: 0.745 V *vs.* RHE) among all RW@Z8(x) catalysts pyrolyzed within the temperature range of 800–1100 °C. This clearly demonstrated that five times the weight loading of the ZIF-8 and the heat-treated temperature around 1000 °C are the optimal conditions in our catalyst preparation procedure. The main reason is likely due to the fact

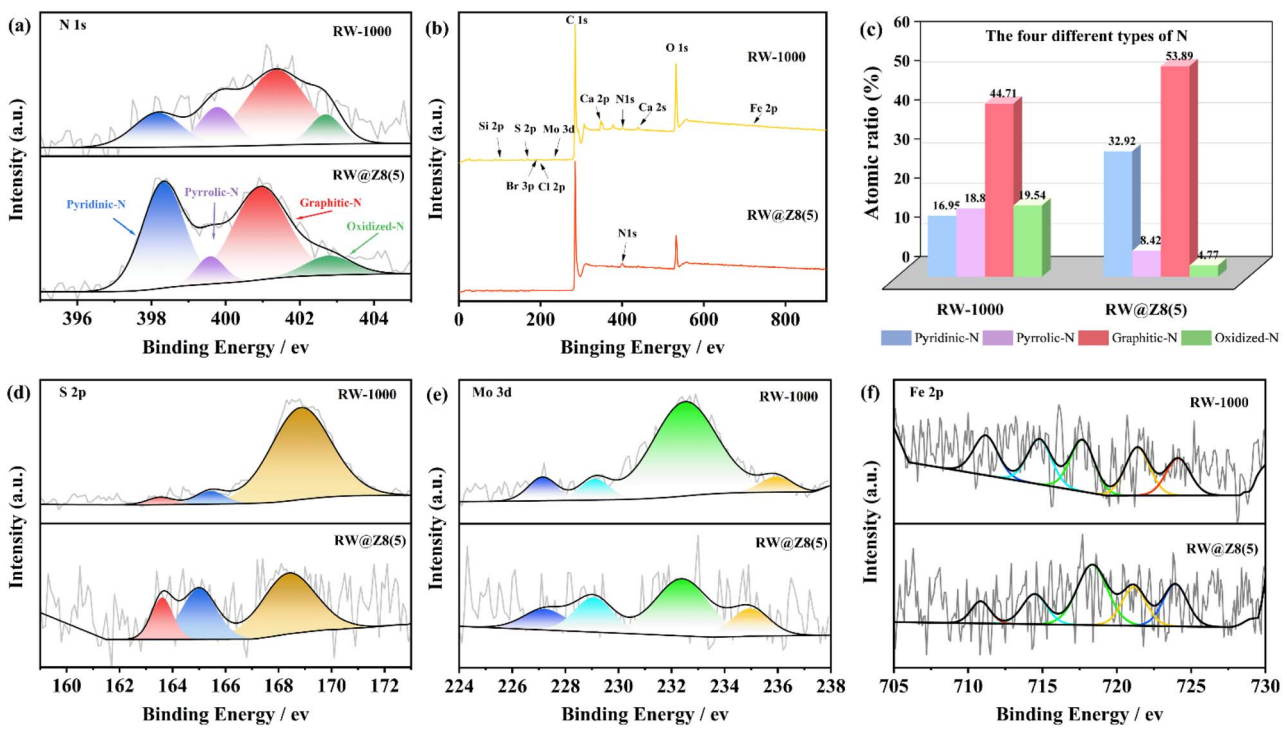

Fig. 4 (a) High-resolution N1s spectra of RW-1000 and RW@Z8(5). (b) The full XPS spectra of RW@Z8(5) and RW-1000. (c) The atomic ratios of the four different species of N in the above catalysts. (d) High-resolution S 2p spectra. (e) High-resolution Mo 3d spectra. (f) High-resolution Fe 2p spectra.

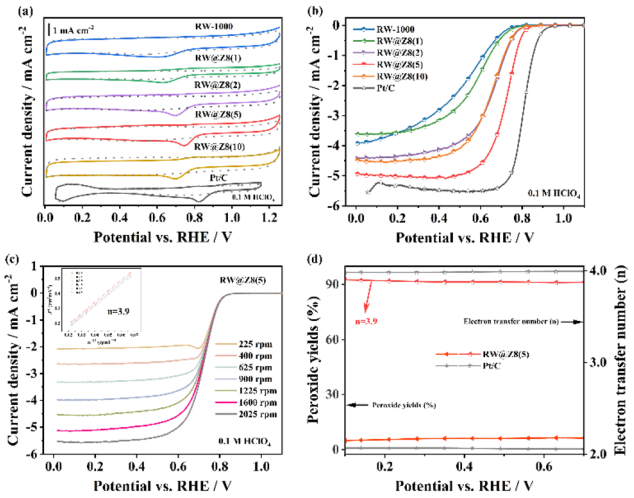

Fig. 5 (a) CV curves of RW-1000, RW@Z8(x) (x = 1,2,5, and 10), and Pt/C in O_2 or N_2-saturated 0.1 M $HClO_4$ solution at a scanning rate of 10 mV s^{-1}. (b) Corresponding LSV curves in O_2-saturated 0.1 M $HClO_4$ solution at a scan rate of 10 mV s^{-1} and a rotation speed of 1600 rpm. (c) LSV curves of RW@Z8(5) at a different rotation speed from 225 to 2025 rpm, and the inset shows the K–L plots in the potential range of 0.1 to 0.6 V. (d) Peroxide yield (%) and electron transfer number (n) of RW@Z8(5) and Pt/C in O_2-saturated 0.1 M $HClO_4$ solution at different potentials, which were calculated by the corresponding RRDE dates.

that the Zn in ZIF-8 starts to evaporate around 900 °C,[39,52] which promotes the formation of more cavities and an increased specific surface area. However, the higher pyrolysis temperatures may further anneal the carbon material, causing the pores to collapse and reducing the catalyst's ORR catalytic efficiency. The attempt to verify the role of the nodules from different bean roots and produced places is also tried. The ORR performance of the RW-derived catalyst exhibited the highest activity among catalysts derived from different bean roots, including White lentil (W), Soybean (S), Lentil (L), and Knife bean (K).

We employed the rotating disk electrode (RDE) method to test the catalyst RW@Z8(5) using linear scanning voltammetry (LSV) in order to further examine its electrocatalytic performance, as shown in Fig. 5b. The maximum half-wave potential ($E_{1/2}$) of the catalyst RW@Z8(5) was 0.720 V (*vs.* RHE) and the limiting diffusion current density (J_L) was 5.08 mA cm^{-2} at 0.1 M $HClO_4$ and at 1600 rpm. Based on the data, we estimated the Tafel slope (Fig. S17†), which reveals that the catalyst RW@Z8(5) has the lowest Tafel slope of 52.59 mV/dec across RN@Z8(x)-T catalysts. The other catalysts made as depicted in Fig. S15–S19† underwent testing for the same electrochemical characteristics. RW@Z8(5) has the lowest.

Fig. 5c shows the LSV curves of RW@Z8(5) from 225 to 2025 rpm. As the rotating speed increases, so does J_L while the diffusion distance decreases. The average electron transfer number was calculated to be 3.9 using the K–L equation, showing that the reaction follows a highly selective four-electron transfer comparable to that of the Pt/C catalyst. The rotating ring disk electrode (RRDE) tests in 0.1 M $HClO_4$ at 1600 rpm and a ring potential of 1.2 V were used to further assess the ORR catalytic pathway. Over a broad voltage range, the average electron transfer number of RW@Z8(5) was 3.9, and the perovskite yield ranged from 5.0% to 6.45%. The electron transfer number is comparable to that of Pt/C and matches the value derived from the K–L curve.

In the performance evaluation of fuel cell catalysts, besides electrochemical activity, methanol tolerance and catalyst durability are also crucial parameters. In order to assess the methanol tolerance of RW@Z8(5) and Pt/C, *i–t* chronoamperometric measurements were performed in O_2-saturated 0.1 M $HClO_4$ at 1600 rpm and a constant voltage of 0.6 V, as shown in Fig. 6c. In acidic conditions, the RW@Z8(5) catalyst shows negligible change in current before and after the injection of 1 M methanol, while Pt/C experiences a significant current decay after methanol addition. This demonstrates that RW@Z8(5) exhibits superior methanol resistance compared to Pt/C catalysts under acidic conditions. This is mostly because the electrochemical process oxidizes methanol on the Pt surface, competing with the original ORR. By adhering to the Pt surface and creating a link that takes up several active sites, the CO generated by methanol oxidation lowers catalytic activity. The same test parameters were used to perform i-t chronoamperometric tests to evaluate the durability of RW@Z8(5) and Pt/C in 30 000 s, as shown in Fig. 6b. The RW@Z8(5) and Pt/C retained 79.22% and 51.05% of their original current density. The RW@Z8(5) and Pt/C showed a general 79.22% and 51.05% durability of the original current density, respectively. These results also show that RW@Z8(5) in acidic environments has better long-term stability compared to commercially available Pt/C.

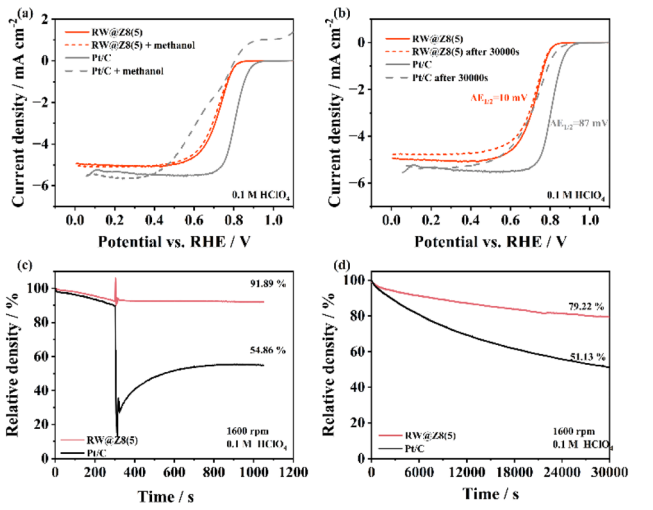

Fig. 6 (a) LSV curves of RW@Z8(5) and Pt/C in O_2-saturated 0.1 M $HClO_4$ solution at a rotation speed of 1600 rpm with/without 1 M methanol; (b) LSV curves of RW@Z8(5) and Pt/C before and after 30 000 s durability measurement in O_2-saturated 0.1 M $HClO_4$ solution at a rotation speed of 1600 rpm; (c) chronoamperometric responses of RW@Z8(5) and Pt/C at 0.6 V in O_2-saturated 0.1 M $HClO_4$ solution at a rotating rate of 1600 rpm with 1 M methanol added at 300 s; (d) Current–time (*i–t*) durability measurement for RW@Z8(5) and Pt/C at 0.6 V in O_2-saturated 0.1 M $HClO_4$ solution with slight bubbling at a rotating rate of 1600 rpm.

Conclusions

In summary, an eco-friendly and atom-economical strategy has been developed to synthesize the highly efficient ORR catalysts using ZIF-8 as an activator and the legume root nodules as the precursor. The porous carbon materials doped with bimetal (Mo, Fe) and heteroatoms (N, S) were obtained by this strategy. The highest specific surface area of these catalysts reaches 1459.27 $m^2 g^{-1}$. The half-wave potential of the optimal catalyst was only just 88 mV behind the commercially available Pt/C catalyst. Our data indicate that the ORR performance of the final catalysts is mainly influenced by the loading of ZIF-8, heat treatment temperature, Fe/Mo elemental content, and multi-layer pore structure. The current strategy also proves that ZIF-8 can replace the harsh chemical $ZnCl_2$ as an activator, avoiding environmental problems such as acid wash treatment and high salt wastewater discharge, creating a new avenue for the atom-economical and sustainable utilization of biomass.

Data availability

The data supporting this article have been included as part of the ESI.†

Author contributions

Supervision, Minyu Li, Wenmu Li; experiment plan, Yifan Zhou; material preparation, Yifan Zhou; electrochemical measurements, Yifan Zhou; data analysis, Yifan Zhou and Minyu Li; writing – original draft, Yifan Zhou and Minyu Li; revising the draft, Wenmu Li and Minyu Li; Minyu Li, Yifan Zhou, Lingling Lin and Wenmu Li, writing – review & editing.

Conflicts of interest

There are no conflicts to declare.

Acknowledgements

This work was supported by the Fujian Science and Technology Innovation Laboratory for Optoelectronic information of China (2021ZZ107), the Science and Technology Service Network Plan of the Chinese Academy of Sciences (2023T3093), and the Natural Science Foundation of Fujian Province (2024J01930).

Notes and references

1 B. Zhang, Y. Jiang and R. Balasubramanian, *J. Mater. Chem. A*, 2021, **9**, 24759–24802.
2 J. Wang, P. Nie, B. Ding, S. Dong, X. Hao, H. Dou and X. Zhang, *J. Mater. Chem. A*, 2017, **5**, 2411–2428.
3 A. Dessalle, J. Quílez-Bermejo, V. Fierro, F. Xu and A. Celzard, *Carbon*, 2023, **203**, 237–260.
4 X. Wang, J. Fang, X. Liu, X. Zhang, Q. Lv, Z. Xu, X. Zhang, W. Zhu and Z. Zhuang, *Sci. China Mater.*, 2019, **63**, 524–532.
5 J. Xuan, M. K. H. Leung, D. Y. C. Leung and M. Ni, *Renewable Sustainable Energy Rev.*, 2009, **13**, 1301–1313.
6 M. Borghei, J. Lehtonen, L. Liu and O. J. Rojas, *Adv. Mater.*, 2017, **30**, 1703691.
7 H. He, R. Zhang, P. Zhang, P. Wang, N. Chen, B. Qian, L. Zhang, J. Yu and B. Dai, *Adv. Sci.*, 2023, **10**, 2205557.
8 S. Zago, L. C. Scarpetta-Pizo, J. H. Zagal and S. Specchia, *Electrochem. Energy Rev.*, 2024, **7**, 1.
9 S.-H. Park, D.-H. Park, J.-H. Byeon, M.-H. Kim, Y. Gu, D.-M. Lim, J.-H. Kim, J.-S. Jang, C.-E. Hong, D.-G. Seo, J.-I. Han and K.-W. Park, *Carbon*, 2024, **218**, 118666.
10 Y. Cha, T. Kim, K. Kim, J. W. Seo, H. Y. Jang and W. Choi, *Carbon*, 2024, **220**, 118859.
11 L. Shen, J. Ying, K. I. Ozoemena, C. Janiak and X. Y. Yang, *Adv. Funct. Mater.*, 2021, **32**, 2110851.
12 D. Guo, Q. Pan, T. Vietor, W. Lu and Y. Gao, *J. Energy Chem.*, 2023, **87**, 518–539.
13 Y. Guo, Z. Jiang, X. Wang, W. Ying, D. Chen, S. Liu, S. Chen, Z.-j. Jiang and X. Peng, *J. Mater. Chem. A*, 2018, **6**, 19547–19554.
14 Q. Zhai, H. Huang, T. Lawson, Z. Xia, P. Giusto, M. Antonietti, M. Jaroniec, M. Chhowalla, J. B. Baek, Y. Liu, S. Qiao and L. Dai, *Adv. Mater.*, 2024, **36**, 2405664.
15 S. Park, J. Kim and K. Kwon, *Chem. Eng. J.*, 2022, **446**, 137116.
16 B. M. Matsagar, R.-X. Yang, S. Dutta, Y. S. Ok and K. C. W. Wu, *J. Mater. Chem. A*, 2021, **9**, 3703–3728.
17 E. Antolini, *Renewable Sustainable Energy Rev.*, 2016, **58**, 34–51.
18 Q. Niu, K. Gao, Q. Tang, L. Wang, L. Han, H. Fang, Y. Zhang, S. Wang and L. Wang, *Carbon*, 2017, **123**, 290–298.
19 Y. Li, G. Wang, T. Wei, Z. Fan and P. Yan, *Nano Energy*, 2016, **19**, 165–175.
20 J. Mu, Q. Li, X. Kong, X. Wu, J. Sunarso, Y. Zhao, J. Zhou and S. Zhuo, *ChemElectroChem*, 2019, **6**, 4022–4030.
21 Y. Shen and Y. Zhu, *J. Mater. Chem. A*, 2024, **12**, 6211–6242.
22 J. Wang and S. Kaskel, *J. Mater. Chem.*, 2012, **22**, 23710.
23 G. Singh, A. Maria Ruban, X. Geng and A. Vinu, *Chem. Eng. J.*, 2023, **451**, 139045.
24 H. Liu, C. Cheng and H. Wu, *Sci. Total Environ.*, 2021, **790**, 148214.
25 H. Yang, P. Chen, W. Chen, K. Li, M. Xia, H. Xiao, X. Chen, Y. Chen, X. Wang and H. Chen, *Fuel Process. Technol.*, 2022, **230**, 107215.
26 G. Duan, J. Xiao, L. Chen, C. Zhang, S. Jian, S. He and F. Wang, *J. Energy Storage*, 2023, **67**, 107559.
27 M. Sevilla, N. Díez and A. B. Fuertes, *ChemSusChem*, 2020, **14**, 94–117.
28 N. Díez, A. B. Fuertes and M. Sevilla, *Energy Storage Mater.*, 2021, **38**, 50–69.
29 F. Liu, H. Peng, X. Qiao, Z. Fu, P. Huang and S. Liao, *Int. J. Hydrogen Energy*, 2014, **39**, 10128–10134.
30 F. Jiang, Y. Yao, B. Natarajan, C. Yang, T. Gao, H. Xie, Y. Wang, L. Xu, Y. Chen, J. Gilman, L. Cui and L. Hu, *Carbon*, 2019, **144**, 241–248.
31 D. Gu, Y. Zhou, R. Ma, F. Wang, Q. Liu and J. Wang, *Nanomicro Lett.*, 2017, **10**, 1–12.
32 R. Su, X. Tao, K. Zheng, L. Jiao, C. Zhang, R. Yang, H. Xie, X. Meng and C. Xu, *Carbon*, 2024, **225**, 119125.

33 T. Yue, H. Sui, J. Jia, Y. Chang, S. Guo, Y. Su and M. Jia, *Appl. Catal., B*, 2025, **361**, 124618.
34 Q. Wang and D. Astruc, *Chem. Rev.*, 2019, **120**, 1438–1511.
35 Y. Zeng, C. Li, B. Li, J. Liang, M. J. Zachman, D. A. Cullen, R. P. Hermann, E. E. Alp, B. Lavina, S. Karakalos, M. Lucero, B. Zhang, M. Wang, Z. Feng, G. Wang, J. Xie, D. J. Myers, J.-P. Dodelet and G. Wu, *Nat. Catal.*, 2023, **6**, 1215–1227.
36 J. Lian, J. Y. Zhao, X. M. Wang and Q. Bai, *Carbon*, 2023, **213**, 118257.
37 B. Chi, L. H. Zhang, X. X. Yang, Y. C. Zeng, Y. J. Deng, M. R. Liu, J. L. Huo, C. Z. Li, X. R. Zhang, X. D. Shi, Y. J. Shao, L. Gu, L. R. Zheng, Z. M. Cui, S. J. Liao and G. Wu, *ACS Catal.*, 2023, **13**, 4221–4230.
38 X. Wan, X. Liu, Y. Li, R. Yu, L. Zheng, W. Yan, H. Wang, M. Xu and J. Shui, *Nat. Catal.*, 2019, **2**, 259–268.
39 Y. Wu, G. Liang, D. Chen, Z. Li, J. Xu, G. Huang, M. Yang, H. Zhang, J. Chen, F. Xie, Y. Jin, N. Wang, S. Sun and H. Meng, *ACS Appl. Mater. Interfaces*, 2021, **13**, 48923–48933.
40 A. Mehmood, M. Gong, F. Jaouen, A. Roy, A. Zitolo, A. Khan, M.-T. Sougrati, M. Primbs, A. M. Bonastre, D. Fongalland, G. Drazic, P. Strasser and A. Kucernak, *Nat. Catal.*, 2022, **5**, 311–323.
41 S. Xiao, L. Ma, W. An and P. Shen, *Sep. Purif. Technol.*, 2025, **354**, 129007.
42 M. Lefèvre, E. Proietti, F. d. r. Jaouen and J.-P. Dodelet, *Science*, 2009, **324**, 71–74.
43 Y. He, S. Liu, C. Priest, Q. Shi and G. Wu, *Chem. Soc. Rev.*, 2020, **49**, 3484–3524.
44 S. Yin, Y. Li, J. Yang, J. Liu, S. Yang, X. Cheng, H. Huang, R. Huang, C. T. Wang, Y. Jiang and S. Sun, *Angew. Chem., Int. Ed.*, 2024, **63**, e202404766.
45 W. Wan, Q. Wang, L. Zhang, H.-W. Liang, P. Chen and S.-H. Yu, *J. Mater. Chem. A*, 2016, **4**, 8602–8609.
46 H. Zhou, J. Zhang, I. S. Amiinu, C. Zhang, X. Liu, W. Tu, M. Pan and S. Mu, *Phys. Chem. Chem. Phys.*, 2016, **18**, 10392–10399.
47 J. Zheng, C. Lai, W. Chen, C. Liu, T. Yuan, J. Lv, B. Zhao, D. Dang, G. Long, T. Wang and X. Han, *Small*, 2025, 2411894.
48 M. Hao, R. Dun, Y. Su, L. He, F. Ning, X. Zhou and W. Li, *J. Mater. Chem. A*, 2021, **9**, 14331–14343.
49 R. D. Milton and S. D. Minteer, *Acc. Chem. Res.*, 2019, **52**, 3351–3360.
50 S. Burén, E. Jiménez-Vicente, C. Echavarri-Erasun and L. M. Rubio, *Chem. Rev.*, 2020, **120**, 4921–4968.
51 L. Voß, K. J. Heinemann, M. Herde, N. Medina-Escobar and C.-P. Witte, *Nat. Commun.*, 2022, **13**, 5331.
52 L. Yang, X. Zeng, W. Wang and D. Cao, *Adv. Funct. Mater.*, 2017, **28**, 1704537.